Chip-to-chip quantum teleportation and multi-photon entanglement in silicon

Chip-to-chip quantum teleportation and multi-photon entanglement in silicon

Daniel Llewellyn[1,†], Yunhong Ding[2,3,†], Imad I. Faruque[1,†], Stefano Paesani[1], Davide Bacco[2,3], Raffaele Santagati[1], Yan-Jun Qian[4], Yan Li[4,5], Yun-Feng Xiao[4,5,6], Marcus Huber[7], Mehul Malik[8], Gary F. Sinclair[1], Xiaoqi Zhou[9], Karsten Rottwitt[2,3], Jeremy L. O'Brien[1], John G. Rarity[1], Qihuang Gong[4,5,6], Leif K. Oxenlowe[2,3], Jianwei Wang[1,4,5,6,⋆], Mark G. Thompson[1]

[1] *Quantum Engineering Technology Labs, H. H. Wills Physics Laboratory and Department of Electrical and Electronic Engineering, University of Bristol, BS8 1FD, Bristol, United Kingdom*

[2] *Department of Photonics Engineering, Technical University of Denmark, 2800 Kgs. Lyngby, Denmark*

[3] *Center for silicon Photonics for Optical Communication (SPOC), Technical University of Denmark, 2800 Kgs. Lyngby, Denmark*

[4] *State Key Laboratory for Mesoscopic Physics, School of Physics, Peking University, Beijing, 100871, China.*

[5] *Frontiers Science Center for Nano-optoelectronics & Collaborative Innovation Center of Quantum Matter, Peking University*

[6] *Beijing Academy of Quantum Information Sciences, West Bld.3,No.10 Xibeiwang East Rd., Haidian District, Beijing 100193,China*

[7] *Institute for Quantum Optics and Quantum Information (IQOQI), Austrian Academy of Sciences, Vienna, Austria*

[8] *Institute of Photonics and Quantum Sciences (IPaQS), Heriot-Watt University, Edinburgh, UK*

[9] *State Key Laboratory of Optoelectronic Materials and Technologies and School of Physics, Sun Yat-sen University, Guangzhou, China*

[†] *These authors contributed equally to this work.* [⋆] *Email: jww@pku.edu.cn*

Integrated optics provides a versatile platform for quantum information processing and transceiving with photons [1–8]. The implementation of quantum protocols requires the capability of generating multiple high-quality single-photons and processing photons with multiple high-fidelity operators [9–11]. Previous experimental demonstrations however present major challenges in realising sufficiently high-quality multi-photon sources and multi-qubit operators in a single integrated system [4–8], and thus fully chip-based implementations of multi-qubit quantum tasks remain a significant challenge [1–3]. Here we report the demonstration of chip-to-chip quantum teleportation and genuine multi-partite entanglement, the core functionalities in quantum technologies, on silicon photonic circuitry. Four single-photons with high purity and indistinguishablity are produced in an array of microresonator sources, without requiring any spectral filtering. Up to four qubits are processed in a reprogrammable linear-optic quantum circuit that facilitates Bell-projection and fusion-operation. The generation, processing, transceiving and measurement of multi-photon multi-qubit states are all achieved in micrometer-scale silicon chips, fabricated by the complementary metal-oxide-semiconductor process. Our work lays the groundwork for large-scale integrated photonic quantum technologies for communications and computations.

Entanglement and teleportation are the backbone of quantum technologies [9–14]. Photons are unique in their capabilities to transmit quantum information over long distances and process quantum information with low noise, positioning entanglement and teleportation of photonic qubits in the heart of quantum communications, quantum networks and quantum computations. For example, quantum communication networks [15] – where small-scale quantum processors are coherently connected via quantum channels, are based on the long-range distribution of multi-photon entangled states and the teleportation of qubit states [12, 13]. In the Knill-Laflamme-Milburn optical quantum computing scheme [9], the teleportation of non-deterministic entangling gates allows an efficient improvement of the success probability [14]. Measurement-based quantum computing models, more resource-efficient for optical quantum computing [10], are fully based on the cluster entangled states and the teleportation of logical operations between qubit sites.

Integrated photonics provides a versatile platform for quantum information processing and communications [16]. Previous demonstrations have shown large integration of two-photon sources and circuits [6], as well as precise control of photonic states [3]. However, the difficulties in realising high-performance multi-photon sources and multi-qubit operators presents major challenges in implementing advanced quantum tasks. Here, by developing state-of-the-art multi-photon multi-qubit quantum devices in silicon, we demonstrated the chip-to-chip quantum teleportation of arbitrary single-qubit states and the generation of four-photon four-qubit Greenberger-Horne-Zeilinger (GHZ) genuine entangled states.

In silicon, single-photons can be generated in *cm*-length waveguides via the spontaneous four-wave mixing (SFWM) process [6–8]. The produced photon-pairs however are highly correlated in frequency [17], and improving their spectral purity requires narrowband spectral filtering – causing a significant reduction of photon rates and heralding efficiency. The waveguide-sources thus have fundamental challenges in scaling up to multi-photon implementations [7, 8, 18]. Instead, microring resonators (MRRs) have been proposed for the generation of single-photons with high spectral purity [19], and high heralding efficiency by removing the requirement of spectral filtering process [20]. Though MRRs have been adopted to produce two-photon [4, 21] and multi-photon states [5, 22], they have not yet been used to demonstrate single-photons having high level of purity, indistinguishablity and heralding efficiency. In addition, when using waveguide-sources, photons are generated uniformly in sources and also circuits [6–8], which induces noise in quantum operations. Locally enhancing the SFWM using MRRs can greatly suppress the noise outside of the MRRs by using a weak pump light. In this work, we realised an array of MRRs to generate multiple high-quality single-photons, which are monolithically integrated with linear-optic circuits that process multiple qubits with high-fidelity and low-noise.

Photonic qubit-qubit interactions are based on quantum interference and success of measurement [9]. It has enabled the demonstrations of controlled-Z operation [1] and single-chip teleportation [2] in the silica platform. However, a full integration of multi-photon sources and multi-qubit operators in this system remains a major challenge. Our chip-to-chip teleportation was realised between two separate silicon chips, and the measured state fidelities are among the highest ones reported so far [11], owing to a full integration of all necessary components with high performance (see Figs. 1a,b). Recently, a similar scheme for three-photon GHZ entanglement has been theoretically proposed using MRRs and circuits, though its further scaling ability may be challenging [23]. In our device (see Fig. 1a), four-photon four-qubit GHZ genuine states were generated and certified, and can be further scaled up to a larger system.

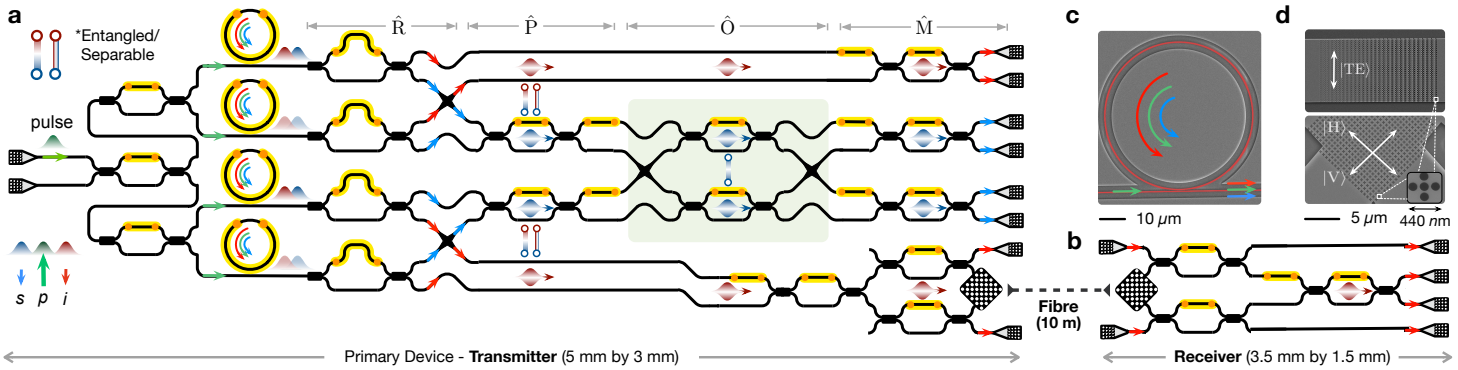

Figure 1 Microresonator-enhanced multi-photon multi-qubit quantum devices in silicon. (**a**) Schematic for the multi-qubit entanglement generator, or the teleportation transmitter. It integrates a network of nonlinear multi-photon sources and linear-optic multi-qubit circuits. Two pairs of nondegenerate photons (red idler, blue signal) are generated in an array of four MRR single-photon sources. Small blue/red circles (photons) with colored links indicate whether the two photons are entangled or separable. The MRRs allow high count-rate, pure, and indistinguishable photon generation while also suppressing background noise from all waveguides and linear circuits. A linear-optic quantum circuit ($\hat{O}$) is programmed to work as a bosonic Bell operator and a fusion entangling operator on the two blue photons. The four photons are demultiplexed by asymmetric MZIs and routed via waveguide-crossers ($\hat{R}$). An array of MZIs and phase-shifters allow the preparation ($\hat{P}$) and projective measurement ($\hat{M}$) of multi-qubit states. Yellow parts refer to electronically controllable thermal-optic phase-shifters. (**b**) Schematic for the teleportation receiver. The transmitter and receiver are coherently linked by a 10m single-mode fiber. The bottom idler qubits in the transmitter can be switched to implement either single-chip (via 1D SGCs) or chip-to-chip (via 2D SGCs) tasks. The receiver chip converts polarisation-encoded qubits to path, which are subsequently measured on the device. (**c**) The scanning electron microscope (SEM) images of a MRR single-photon source coupled to a bus-waveguide (pseudo red colour), and (**d**) metasurface-assisted low-loss SGC with bonded aluminium reflectors. Top: 1D SGC for fiber-chip interface, bottom: 2D SGC for path-polarisation conversion, and inset: zoom-in view of a metasurface cell. White arrows denote the polarised state of photon.

Figure 1 shows the multi-photon multi-qubit devices that are fabricated on the Silicon-on-Insulator platform. The Si MRR-sources array (see SEM image in Fig. 1c) can produce two pairs of signal (λ_s) & idler (λ_i) photons via the SFWM. Four dual-rail qubits are encoded in the four generated photons. Each qubit is represented in the logical basis $\{|0\rangle_k, |1\rangle_k\}$ ($k = 1,2,3,4$) and can be prepared ($\hat{P}$) and measured ($\hat{M}$) by a network of Mach-Zehnder interferometers (MZI) and phase-shifters. Another key component is the reprogrammable two-qubit operator ($\hat{O}$) that can entangle two qubits (previously never interacted) in two different manners, i.e, Bell-projection and fusion-operation. The MRR sources, qubit-generator, entangling-operator, and qubit-analyser are all individually controllable and fully programmable. To preserve coherent teleportation between the transmitter and receiver chips, we exploit a polarisation-path conversion technique relying on the 2D subwavelength grating couplers (SGC) (see SEM image in Fig. 1d). The chips are coupled to optical fibers via an array of 1D SGC [24] (Fig. 1d), and then photons are detected off-chip by 8 superconducting single-photon detectors (∼0.85 efficiency). Details on device and setup are provided in Supplementary Information Sec. 1.

As shown in Fig. 2b, the generated two-photon rate is enhanced by a factor of ∼43 when MRR is on/off resonance. For each MRR, a raw rate of ∼20 kcts/s at a coincidences-to-accidentals ratio ∼50 was detected, using a pump laser with 15 ps pulse width with 500 MHz repetition rate at 800 μW power. Since the MRR sources only require weak pump, negligible photons are created in surrounding waveguides and circuits, greatly suppressing noise there. We further measured the photon-number purity of the single-photons, by performing the Hanbury-Brown-Twiss measurement of photon to obtain the heralded second-order correlation $g^{(2)}(0)$. At the same power, we observed $g^{(2)}(0) = 0.05$ corresponding to 95% photon-number purity (Fig. 2c). A high heralding efficiency of ∼50% after the resonators was measured.

The four MRRs are designed to be identical. The high-yield fabrication enables nearly identical free-spectral-ranges (FSRs∼400 GHz, Fig. 2a) and high spectral overlap at resonances (Fig. S5). Each MRR can be individually tuned and frequency-locked (see Supplementary Information Sec. 2), ensuring photon wavefunctions that are highly overlapped in spectral mode. The photon indistinguishability is estimated by the visibility of heralded two-photon quantum interference. We interfere two signal photons on a MZI (heralding two idler photons), which are emitted from two independent MRRs. Figure 2e reports a quantum interference fringe having multi-pair corrected visibility of 90.99± 3.91%, which agrees within error of the fundamental limit of 92% spectral purity for our MRR design. The asymmetric modulation in the fringe is due to the use of imperfect beamsplitters [22] (see discussions in Supplementary Information Sec. 2). In Fig. 2d, the raw uncorrected visibility as a function of the mean photon number per pulse ($\bar{n}$) is measured, e.g, obtaining ∼84% raw visibility at $\bar{n} = 0.05$. Figure 2f shows the pairwise indistinguishability of the four MRR sources, having a mean raw visibility of $71.9 \pm 2.4\%$ in a high pumping configuration, which if multi-pair corrected, reaches to 87.3 ± 1.9 mean visibility. Remarkably, in all of our indistinguishability measurements, we have not used any spectral filtering process to improve the spectral purity. The MRR sources demonstrate significantly better performance compared with the waveguide sources (see quantitative analysis in Supplementary Information Sec. 2).

The MRR-source array is programmed to create either entangled or separable bipartite states, by controlling the pump excitation in MRRs and re-configuring asymmetric MZIs. When the operator $\hat{O}$ between qubits 2,3 is turned off (see Fig. 3a) the original bipartite states from the MRRs array are measured. We implement quantum state tomography (QST) to reconstruct the density matrix ρ. As examples, Figures 3d,e show the measured ρ for separable states $|10\rangle_{2,3}$ and $|{+}{+}\rangle_{2,3}$ with fidelities of 0.964 ± 0.072 and 0.966 ± 0.024, respectively. The fidelity is defined as $F = \langle\psi_0|\,\rho\,|\psi_0\rangle$, where $|\psi_0\rangle$ is the ideal state. We simultaneously prepared and measured two Bell pairs $|\Phi\rangle^+_{1,2}$ and $|\Phi\rangle^+_{3,4}$ from the four MRRs, having fidelities of 0.917 ± 0.002 and 0.915 ± 0.003, respectively.

We then exploit a single programmable circuit to implement two key multi-qubit operations in quantum applications, i.e., entangling

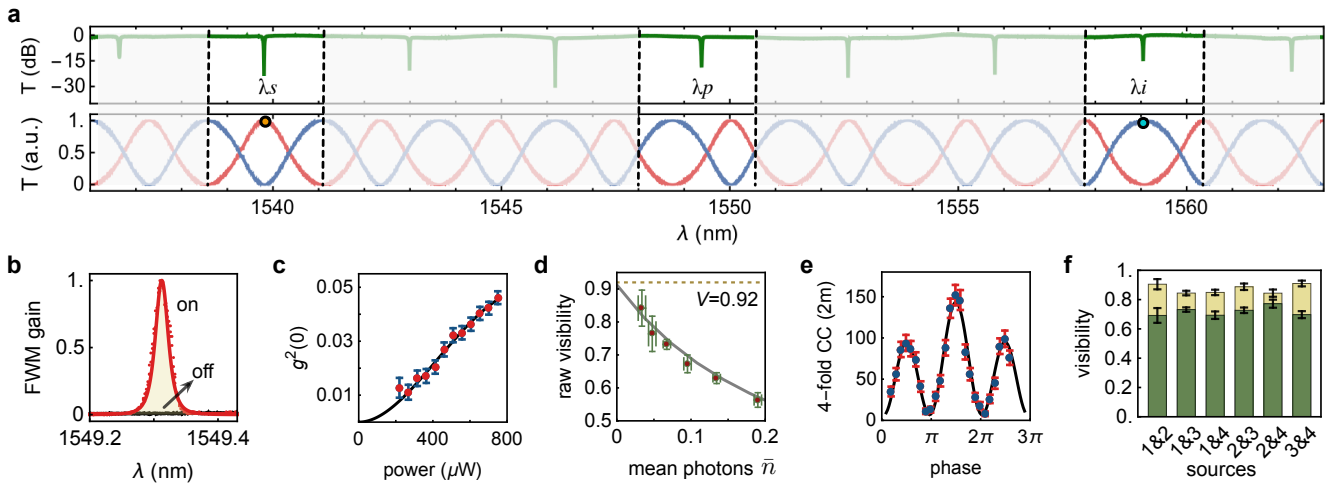

Figure 2 Photon-pair generation in an array of microresonator nonlinear sources. (**a**) The measured transmission spectra for an MRR (top) and asymmetric MZI (bottom), where FSR_{MRR}= 400 GHz and FSR_{AMZI}= 320 GHz. Signal photons are created at λ_s= 1539.758 nm and idler photons at λ_i= 1559.015 nm, with a pump light at λ_p= 1549.30 nm, all at the resonances of MRR. Asymmetric MZIs can demultiplex the λ_s and λ_i photons. Residual pump photons are removed by off-chip filters with a ∼1.1 nm bandwidth, much wider than the linewidth of MRRs 37.7 ± 1.9 pm. (**b**) FWM enhancement in MRR when on resonance. Background noise in the whole device is efficiently suppressed (off-resonance). (**c**) Tests of photon number purity by measuring the heralded $g^{(2)}(0)$. (**d**) Measured raw visibility of the heralded quantum interference, as a function of mean photon number $\bar{n}$ per pulse. The V = 0.92 dotted line is the maximum achievable visibility for our MRR designs. (**e**) Tests of spectral indistinguishability, with a subtraction of multi-pair events. Visibility of 90.99 ± 3.91% are obtained, agreeing with the theoretical limit. (**f**) Measured visibility of quantum interference between pairwise MRRs in the array. Mean visibilities of 87.3 ± 1.9% and 71.9 ± 2.4% are measured, with and without multi-pair corrections. Points are all experimental data, while lines in (d) are theoretical values, and lines in (b, c, and e) are fittings. All error bars refer to ±1 standard deviation (s.d.) estimated from Poissonian photon-counting statistics.

initially separable qubits and measuring qubits in the Bell basis. Figure 3b,c show the diagrams for the bosonic Bell projector $\hat{O}_{Bell}$ and fusion operator $\hat{O}_{fusion}$ that are devised for dual-rail qubits. We here study a case where the state $|0\rangle^{\otimes 4}$ is initially prepared, then $\rho_{2,3}$ is processed with the herald of photons 1, 4. The $\hat{O}_{Bell}$ is capable of distinguishing the Bell states $|\Psi\rangle^{\pm}$ from the others. We distinguish $|\Psi\rangle^{+}$ when observing joint clicks in {D3, D4} or {D5, D6} (Fig. 3a,b). The $\hat{O}_{fusion}$ transmits $|0\rangle$ and swaps $|1\rangle$ mode, able to fuse a two-qubit separable state into an entangled state when detecting only one photon in {D3, D4} and another in {D5, D6} (Fig. 3a,c). To verify these new on-chip building-blocks, heralded quantum interference and Bell state generation are performed. Figure 3f reports the two-qubit ($|10\rangle_{2,3}$) interference, gradually rotating the qubit 2 around the $\hat{\sigma}_y$ axis. The observed 80.5 ± 3.2% visibility confirms high quality interference of two bosons at $\hat{O}_{Bell}$. Figure 3g shows the two-qubit (input $|{+}{+}\rangle_{2,3}$) interference at $\hat{O}_{fusion}$ having a 85.8 ± 4.4% visibility, when rotating the qubit 2 around the $\hat{\sigma}_z$ axis. In general, performing $\hat{O}_{Bell}$ and $\hat{O}_{fusion}$ enables the generation of entangled states, transforming the state $|10\rangle_{2,3}$ (Fig. 3d) to $|\Psi\rangle^{-}_{2,3}$ (Fig. 3h), and $|{+}{+}\rangle_{2,3}$ (Fig. 3e) to $|\Phi\rangle^{+}_{2,3}$ (Fig. 3i). We obtained entangled state having fidelities of 0.851 ± 0.040 and 0.830 ± 0.032, respectively. More details are provided in Supplementary Information Sec. 3.

In the teleportation protocol, an unknown quantum state can be transmitted to another location, by locally collapsing the state and remotely reconstructing it [11]. This requires access to Bell states and Bell measurements. The single-chip teleportation experiment was initially implemented (see Fig. 1a), where we prepared an arbitrary single-qubit state $|\psi\rangle_2$ in photon 2 ("B") via a unitary $\hat{P}$, and a Bell pair $|\Phi\rangle^{+}_{3,4}$ in photon 3 ("C") and photon 4 ("D"). Photon 1 ("A") was used as a trigger. The $\hat{O}_{Bell}$ measurement was performed at B and C, projecting the state into $|\Psi\rangle^{+}_{2,3}$ basis. This process allows the teleportation of B's state $|\psi\rangle_2$ to D up to a local rotation $\hat{\sigma}_x$. We prepared six different $|\psi\rangle_2$ states at B and reconstructed at D obtaining $|\phi\rangle_4$. Full QST was implemented to reconstruct density matrices for the six $|\phi\rangle_4$ states, see experimental data in Fig. S12. On a single chip, we obtained high-fidelity teleported states with a mean $\bar{F} = 0.906 \pm 0.014$.

We then implemented the chip-to-chip teleportation. We ensured the preservation of coherent teleportation between two chips using the path-polarisation conversion technique [25]. In our experiments, the $|\Phi\rangle^{+}_{3,4}$ state was created on the transmitter (Fig. 1a), and qubit 4 was distributed to the receiver chip (Fig. 1b) via a 10m-long optical fiber. We remark that the states of the entangled channel after distribution remain highly coherent with negligible degradation of fidelity, see full set of distributed entangled states in Fig. S11. The $\hat{O}_{Bell}$ was carried out on the transmitter. We implemented the teleportation of the six pure states, this time between the transmitter and receiver devices, see full data in Fig. 4a. The teleported states $|\phi\rangle_4$ are recovered on the receiver, and QST reports average fidelities of $\bar{F} = 0.885 \pm 0.037$.

Teleportation of entanglement (i.e, entanglement swapping) is a protocol whereby the sets of entanglement, say {A, B} and {C, D}, can be swapped [11]. This means that collapsing {B, C} onto a Bell state will result in the entanglement of {A, D}, which is unique in the sense that {A, D} are not required to have ever interacted with one another. Figure 4b shows the circuit for entanglement swapping, where two Bell pairs $|\Phi\rangle^{+}_{1,2} \otimes |\Phi\rangle^{+}_{3,4}$ are created in the MRRs-array and $\hat{O}_{Bell}$ is performed on the qubits 2, 3, projecting the qubits 1, 4 into the entangled state $|\Psi\rangle^{+}_{1,4}$. Additionally, performing $\hat{O}_{fusion}$ and measuring qubits 2, 3 in the $\hat{\sigma}_x\hat{\sigma}_x$ basis produces the entangled state $|\Phi\rangle^{+}_{1,4}$. We performed QST on qubits 1, 4 and reconstructed $|\Psi\rangle^{+}_{1,4}$ and $|\Phi\rangle^{+}_{1,4}$, each from nine global measurement settings. Figure 4b(ii) reports the measured ρ with fidelities of 0.776 ± 0.018 and 0.737 ± 0.019, respectively, demonstrating successful on-chip entan-

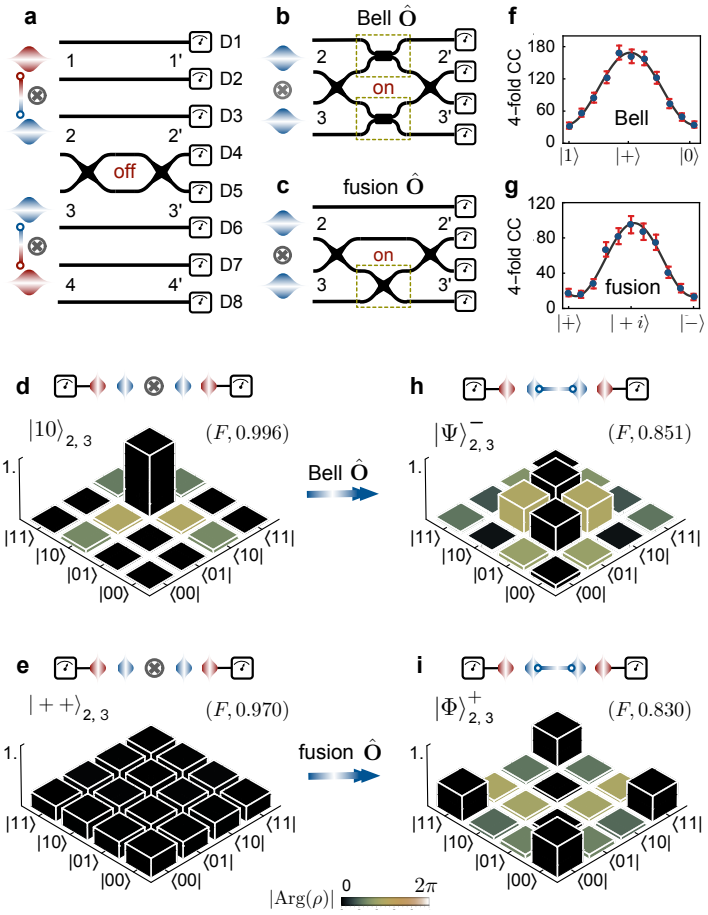

Figure 3 Programmable linear-optic quantum circuits for Bell projection and fusion operation. (**a**) Simplified diagram for a general operator, in this case $\hat{O} = \hat{I}\otimes\hat{I}$ on qubits 2, 3, i.e, $\hat{O}$ is off. Each pair of lines refers to the dual-rail logical state $|0\rangle$ and $|1\rangle$. (**b** and **c**) Diagrams for the Bell operator $\hat{O}_{\text{Bell}}$ and fusion operator $\hat{O}_{\text{fusion}}$ in the spatial mode. For $\hat{O}_{\text{Bell}}$, a photon has 50% probability of being measured in either 2′ or 3′, regardless of its input in 2 or 3. The $\hat{O}_{\text{fusion}}$ transmits $|0\rangle$ and swaps $|1\rangle$ mode. In the dashed boxes the circuits are reconfigured as a Hadamard-like or swap-like operator. The generated states in the source array can be programmed as either bipartite entangled (see Supplementary Information), or separable (**d**) $|10\rangle_{2,3}$ and (**e**) $|++\rangle_{2,3}$ (two red photons are in herald). The values in (*) refer to the measured state fidelity (F) to their ideal states. (**f** and **g**) Quantum interference when the two blue qubits $|10\rangle_{2,3}$ ($|++\rangle_{2,3}$) meet at the $\hat{O}_{\text{Bell}}$ ($\hat{O}_{\text{fusion}}$) and rotate qubit 2 along the $\hat{\sigma}_y$ axis (along the $\hat{\sigma}_z$ axis). Points are experimental data measured in the $\hat{\sigma}_x\hat{\sigma}_x$ basis, and lines are fitted with a sinusoidal function. (**h** and **i**) Reconstructed density matrices for entangled states $\rho_{2,3}$, when performing $\hat{O}_{\text{Bell}}$ ($\hat{O}_{\text{fusion}}$) on the separable states in (d) and (e). Small blue/red pulses indicate different photons in the experiment, whilst joining lines indicate entangled states and $\otimes$ represents separable states. The ρ are reconstructed by performing full QST on-chip. Column heights represent $|\rho|$ while colors represent $|\text{Arg}(\rho)|$. All error bars refer to ±1 s.d. estimated from Poissonian photon-counting statistics.

glement swapping of photonic states for the first time.

We then generated three- and four-photon GHZ entangled states on chip [26]. Performing $\hat{O}_{\text{fusion}}$ on the two Bell pairs $|\Phi\rangle^{+}_{1,2}\otimes|\Phi\rangle^{+}_{3,4}$ enables the fusion between qubits 2 and 3, thus yielding the four-qubit GHZ state $|\Phi\rangle^{n}_{\text{GHZ}} = (|0\rangle^{\otimes n} + |1\rangle^{\otimes n})/\sqrt{2}$, $n = 4$. This entangling process succeeds with a 0.5 probability, when detecting only one photon in each of {D1, D2}, {D3, D4}, {D5, D6} and {D7, D8} (Fig. 4c). The four-photon coincidence events arise from one of the two cases, either all photons are in the $|0\rangle$ mode or in the $|1\rangle$ mode, which are quantum mechanically indistinguishable in the superposition basis and thus results in coherent entanglement. The $|\Phi\rangle^{3}_{\text{GHZ}}$ and $|\Phi\rangle^{2}_{\text{GHZ}}$ (i.e, $|\Phi\rangle^{+}_{1,4}$) states can be produced by locally measuring the remaining qubits in the $\hat{\sigma}_x$ basis.

To verify genuine multipartite entanglement (GME) for the states where all subsystems are genuinely entangled, we measured an entanglement witness operator $\hat{W}_n = \hat{I}/2 - |\Phi^{n}_{\text{GHZ}}\rangle\langle\Phi^{n}_{\text{GHZ}}|$ [27]. Figures 4c reports the probability distribution in the basis $\hat{\sigma}_z^{\otimes n}$, $\hat{\sigma}_x^{\otimes n}$, and the general basis $\hat{\Omega}_\theta^{\otimes n} = (\cos\theta\hat{\sigma}_x + \sin\theta\hat{\sigma}_y)^{\otimes n}$, where $\{\hat{\sigma}_x, \hat{\sigma}_y, \hat{\sigma}_z\}$ are the Pauli operators. The fringes of $\langle\hat{\Omega}_\theta^{\otimes n}\rangle$ show the measured coherence of the GHZ states, and the variable oscillatory frequency confirms the correlation nature of n-photon GHZ entanglement. With a total $n+1$ measurements, we calculated the $F'_{n=3,4}$ fidelities for $|\Phi\rangle^{n}_{\text{GHZ}}$ with values of 0.683 ± 0.014 and 0.735 ± 0.017, and obtained the $\langle\hat{W}\rangle_{n=3,4}$ values of -0.235 ± 0.017 and -0.183 ± 0.014, respectively, certifying the genuine entanglement of the four-photon and three-photon GHZ states with at least 13σ.

We further quantified GME of the generated GHZ states without QST or other assumptions on the state itself using GME-concurrence (C_{GME}) [28], which has computable bounds that turn out to be exact for GHZ-diagonal states. We used an efficient framework to lower bound the GME-concurrence from only two global measurement settings. Using only the outcome statistics of two measurements, $\hat{\sigma}_z^{\otimes n}$ in Fig. 4c(ii) and $\hat{\sigma}_x^{\otimes n}$ in Fig. 4c(iii), we arrive at a value of $C^3_{\text{GME}} \leq 0.390\pm0.04$ and $C^4_{\text{GME}} \leq 0.192\pm0.039$ for three and four-photon GHZ states respectively, thus efficiently quantifying genuine multi-partite entanglement. The two-basis measurements can also be used to efficiently lower bound the state fidelity [29] with values of 0.593 ± 0.019 and 0.693 ± 0.020 for the four- and three-photon states, respectively. See Supplementary Information Sec. 5 for more details on the generation, verification, and quantification of GME.

We have presented state-of-the-art silicon-photonic quantum devices, able to produce, process, transmit and measure multi-photon multi-qubit states. With these devices, chip-based teleportation and genuine multi-photon entanglement have been demonstrated. The achieved teleportation with a ~0.90 fidelity is among the highest seen (see Ref. [11]), owing to the realisations of high-quality multi-photon sources and multi-qubit operators. The photon sources are approaching the optimal levels of photon purity and indistinguishability, while the heralding efficiency can be further improved [20]. With the developed technologies, we expect the generation of 10-photon entangled states is achievable in near future [18]. Our MRRs provides the essential ingredients for integrated multiplexing sources [30], which promises the near-deterministic generation of single-photons. Moreover, with a "near-zero-change" of complementary metal-oxide-semiconductor process, silicon offers the capability of integrating very-large-scale quantum photonic circuits [6]. Our demonstrations pave the way for a complex integration of quantum nonlinear and linear optic devices in silicon, that can find applications in quantum communications [12, 13], quantum-enhanced measurements [31], quantum computing [10, 18], and distributed quantum information processing networks [15].

Data availability

The data represented in Figs. 2-4 are available as source data in Supplementary Data 2-4. All other data that support the plots within this paper and other findings of this study are available from the corresponding author upon reasonable request.

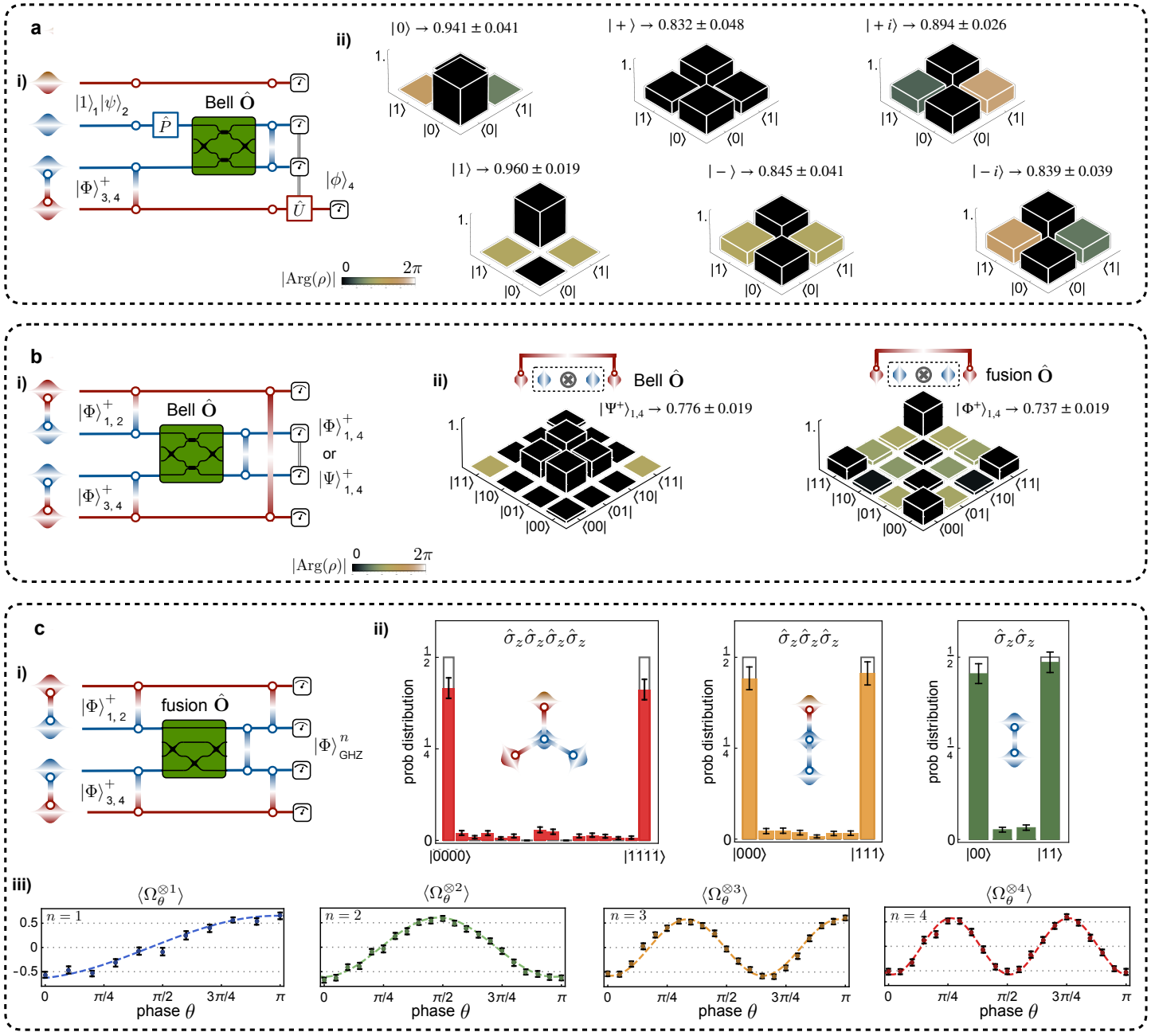

Figure 4 Chip-to-chip quantum teleportation and multi-photon multi-qubit entanglement. Quantum circuit diagrams for: (**a**) teleportation of arbitrary single-qubit states from $|\psi\rangle_2$ to $|\phi\rangle_4$, by performing Bell measurement of qubits 2, 3; (**b**) teleportation (entanglement swapping) of two-qubit entangled states from two Bell pairs $\{|\Phi\rangle^+_{1,2}, |\Phi\rangle^+_{3,4}\}$ to $|\Psi\rangle^+_{1,4}$ or $|\Phi\rangle^+_{1,4}$; (**c**) generation of three-photon and four-photon GHZ entangled states $|\Phi\rangle^n_{\mathrm{GHZ}}$, by fusing $|\Phi\rangle^+_{1,2}$ and $|\Phi\rangle^+_{3,4}$. Each red (blue) line denotes the evolution of one qubit in the logical representation. Small blue/red pulses indicate different photons in the experiment, whilst joining lines indicate entangled states and $\otimes$ represents separable states. (**a, ii**) Experimental results for the chip-to-chip single-qubit teleportation. A full set of six states $\{|0\rangle, |1\rangle, |+\rangle, |-\rangle, |+\mathrm{i}\rangle, |-\mathrm{i}\rangle\}$ was teleported from the transmitter to the receiver, respectively, reporting a mean fidelity of 0.885 ± 0.037. The ρ of six teleported states were reconstructed by full QST on the receiver chip. (**b, ii**) Experimental results for the two-qubit entanglement swapping. Performing $\hat{\mathrm{O}}_{\mathrm{Bell}}$ ($\hat{\mathrm{O}}_{\mathrm{fusion}}$) on $|\Phi\rangle^+_{1,2}$ and $|\Phi\rangle^+_{3,4}$ results in swapped entanglement $|\Psi\rangle^+_{1,4}$ ($|\Phi\rangle^+_{1,4}$) between photons that have not interacted. (**c, ii-iii**) Verification and quantification of GHZ genuine entanglement. Measured four-fold coincidences (normalised) in the (ii) $\hat{\sigma}_z^{\otimes n}$ basis and (iii) $\hat{\sigma}_x^{\otimes n}$ basis for $n = 2, 3, 4$ photons. Grey boxes are theoretical probability distributions. $\{|X\rangle, |\bar{X}\rangle\}$ refers to the $(|0\rangle \pm |1\rangle)/\sqrt{2}$ states. (c, iii) Expectation values of the coherence term $\hat{\Omega}_\theta^{\otimes n}$ for $n = 1, 2, 3, 4$. Each point is derived from a set of 16 four-fold coincidences in the general $(\cos\theta\hat{\sigma}_x + \sin\theta\hat{\sigma}_y)^{\otimes n}$ basis. The fringe in $\theta \in [0, \pi]$ is fitted with a sinusoidal function. All error bars refer to ± 1 s.d. and are estimated from Poissonian photon-counting statistics. Errors in the fidelity of the reconstructed density matrices are estimated using Monte-Carlo simulations of the Poissonian counting statistics.

Code availability

The computer code used for data analysis is available on request from the corresponding author.

References

1. A. Politi, M. J. Cryan, J. G. Rarity, S. Yu & J. L. O'Brien. Silica-on-silicon waveguide quantum circuits. *Science* **320,** 646–649 (2008).

2. B. J. Metcalf *et al.* Quantum teleportation on a photonic chip. *Nature Photonics* **8,** 770–774 (2014).
3. N. C. Harris *et al.* Quantum transport simulations in a programmable nanophotonic processor. *Nature Photonics* **11,** 447–452 (2017).
4. J. W. Silverstone *et al.* Qubit entanglement between ring-resonator photon-pair sources on a silicon chip. *Nature Communications* **6,** 7948 (2015).
5. C. Reimer *et al.* Generation of multiphoton entangled quantum states by means of integrated frequency combs. *Science* **351,** 1176–1180 (2016).
6. J. Wang *et al.* Multidimensional quantum entanglement with large-scale integrated optics. *Science* **360,** 285–291 (2018).
7. M. Zhang *et al.* Generation of multiphoton entangled quantum states with a single silicon nanowire. *Light: Science & Applications* **8,** 41 (2019).
8. J. C. Adcock, C. Vigliar, R. Santagati, J. Siverstone & M. Thompson. Programmable four-photon graph states on a silicon chip. *Nature Communications* **10,** 3528 (2019).
9. E. Knill, R. Laflamme & G. J. Milburn. A scheme for efficient quantum computation with linear optics. *Nature* **409,** 46–52 (2000).
10. M. A. Nielsen. Optical quantum computation using cluster states. *Physical Review Letters* **93,** 040503 (2004).
11. S Pirandola, J Eisert, C Weedbrook, A Furusawa & S. L. Braunstein. Advances in quantum teleportation. *Nature Photonics* **9,** 641–652 (2015).
12. R. Valivarthi *et al.* Quantum teleportation across a metropolitan fibre network. *Nature Photonics* **10,** 676–680 (2016).
13. J.-G. Ren *et al.* Ground-to-satellite quantum teleportation. *Nature* **549,** 70–73 (2017).
14. D. Gottesman & I. L. Chuang. Demonstrating the viability of universal quantum computation using teleportation and single-qubit operations. *Nature* **402,** 390–393 (1999).
15. S. Wehner, D. Elkouss & R. Hanson. Quantum internet: A vision for the road ahead. *Science* **362,** eaam9288 (2018).
16. D. Bonneau, J. W. Silverstone & M. G. Thompson. in *Silicon Photonics III: Systems and Applications* (eds L. Pavesi & D. J. Lockwood) 41–82 (Springer, 2016).
17. W. Grice, A. U'Ren & I. Walmsley. Eliminating frequency and space-time correlations in multiphoton states. *Physical Review A* **64** (2001).
18. S. Paesani *et al.* Generation and sampling of quantum states of light in a silicon chip. *Nature Physics* **15,** 925–929 (2019).
19. Z. Vernon *et al.* Truly unentangled photon pairs without spectral filtering. *Optics Letters* **42,** 3638–3641 (2017).
20. Z. Vernon, M. Liscidini & J. E. Sipe. No free lunch: the trade-off between heralding rate and efficiency in microresonator-based heralded single photon sources. *Optics Letters* **41,** 788–791 (2016).
21. D Grassani *et al.* Micrometer-scale integrated silicon source of time-energy entangled photons. *Optica* **2,** 88–94 (2015).
22. I. I. Faruque, G. Sinclair, D. Bonneau, J. G. Rarity & M. G. Thompson. On-chip quantum interference with heralded photons from two independent micro-ring resonator sources in silicon photonics. *Optics Express* **26,** 20379–20395 (2018).
23. N. Bergamasco, M. Menotti, J. E. Sipe & M. Liscidini. Generation of path-encoded Greenberger-Horne-Zeilinger states. *Physical Review Applied* **8,** 054014 (2017).
24. Y. Ding, C. Peucheret, H. Ou & K. Yvind. Fully etched apodized grating coupler on the SOI platform with -0.58 dB coupling efficiency. *Optics Letters* **39,** 5348–5350 (2014).
25. J. Wang *et al.* Chip-to-chip quantum photonic interconnect by path-polarization interconversion. *Optica* **3,** 407–413 (2016).
26. D. M. Greenberger, M. A. Horne, A. Shimony & A. Zeilinger. Bell's theorem without inequalities. *American Journal of Physics* **58,** 1131–1143 (1990).
27. M. Bourennane *et al.* Experimental detection of multipartite entanglement using witness operators. *Physical Review Letter* **92,** 087902 (8 2004).
28. Z.-H. Ma *et al.* Measure of genuine multipartite entanglement with computable lower bounds. *Physical Review A* **83,** 062325 (2011).
29. J. Bavaresco *et al.* Measurements in two bases are sufficient for certifying high-dimensional entanglement. *Nature Physics* **14,** 1032–1037 (2018).
30. F. Kaneda & K. Paul. High-efficiency single-photon generation via large-scale active time multiplexing. *Science Advances* **5,** eaaw8586 (2019).
31. G. Tóth & I. Apellaniz. Quantum metrology from a quantum information science perspective. *Journal of Physics A: Mathematical and Theoretical* **47,** 424006 (2014).

Author contributions

All authors contributed to the discussion and development of the project. J.W. devised the concept of the experiment. Y.D. designed and fabricated the device. D.L., Y.D., I.F., J.W., S.P., D.B., and R.S. performed the experiment. J.W., D.L., Y.D., I.F., Y. Q., Y.L., Y.X., M.H., M.M., G.F.S., and X.Z. performed the theoretical analysis. K.R., J.L.O., J.G.R., Q.G., L.K.O., Y.D., J. W. and M.G.T. managed the project. The manuscript was written by J.W., D.L., Y.D. and I.F. with the input from all others.

Acknowledgements

We thank G. J. Mendoza and D. Bonneau for useful discussions. We thank W. A. Murray, M. Loutit, E. Johnston, J. W. Silverstone and L. Kling for experimental assistance. We acknowledge support from the Natural Science Foundation of China (nos. 61975001, 61590933, 11527901, 11825402), National Key R&D Program of China (nos. 2018YFB1107205), Beijing Natural Science Foundation (Z190005), Beijing Academy of Quantum Information Sciences (Y18G21) and Key R&D Program of Guangdong Province (2018B030329001). Y.D. acknowledges support from Denmark SPOC (DNRF123), VILLUM FONDEN, QUANPIC (00025298). I.I.F. acknowledges FP7 Marie Curie Initial Training Network PICQUE (608062). M.H. acknowledges support from the Austrian Science Fund (FWF) through the START project (Y879-N27) and the joint Czech-Austrian project MultiQUEST (I 3053-N27, GF17-33780L). M.M. acknowledges support from the Engineering and Physical Sciences Research Council (EPSRC) (EP/P024114/1) and the QuantERA ERA-NET co-fund (FWF Project I3773-N36). K.R. acknowledges the support from the QuantERA. J.L.O. acknowledges a Royal Society Wolfson Merit Award and a Royal Academy of Engineering Chair in Emerging Technologies. M.G.T. acknowledges support from the European Research Council (ERC) starter grant (ERC-2014-STG 640079) and an EPSRC Early Career Fellowship (EP/K033085/1).

Competing interests

M.T. is involved in developing quantum photonic technologies at PsiQuantum Corporation.

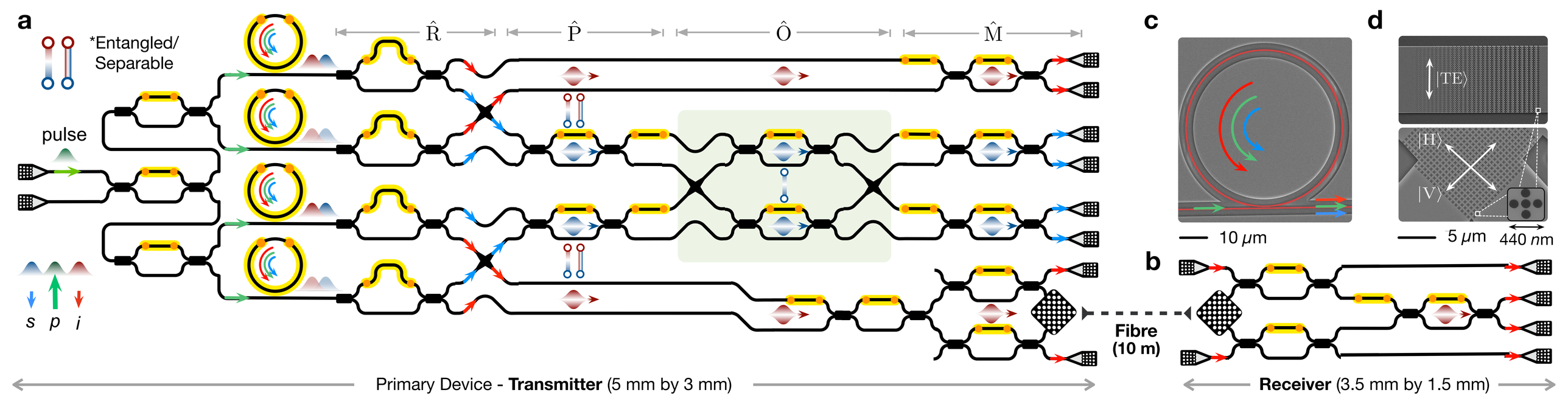
a
*Entangled/
Separable
pulse
s p i
R̂
P̂
Ô
M̂
Fibre
(10 m)
Primary Device - **Transmitter** (5 mm by 3 mm)
b
Receiver (3.5 mm by 1.5 mm)
c
10 μm
d
|TE⟩
|H⟩
|V⟩
5 μm
440 nm

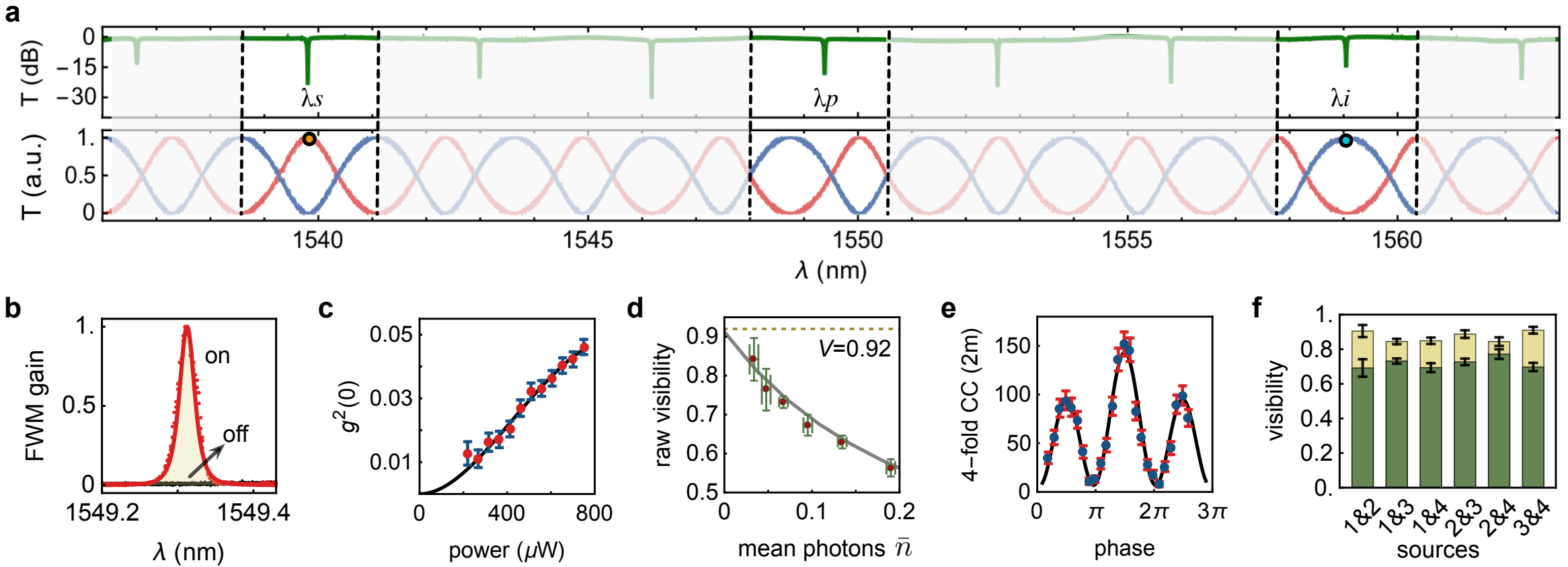
a
T (dB)
0
−15
−30
λs
λp
λi
T (a.u.)
1.
0.5
0
1540
1545
1550
1555
1560
λ (nm)
b
FWM gain
1.
0.5
0
on
off
1549.2
1549.4
λ (nm)
c
g²(0)
0.05
0.03
0.01
0
400
800
power (μW)
d
raw visibility
0.9
0.8
0.7
0.6
0.5
V=0.92
0
0.1
0.2
mean photons n̄
e
4−fold CC (2m)
150
100
50
0
0
π
2π
3π
phase
f
visibility
1.
0.8
0.6
0.4
0.2
0.
1&2
1&3
1&4
2&3
2&4
3&4
sources

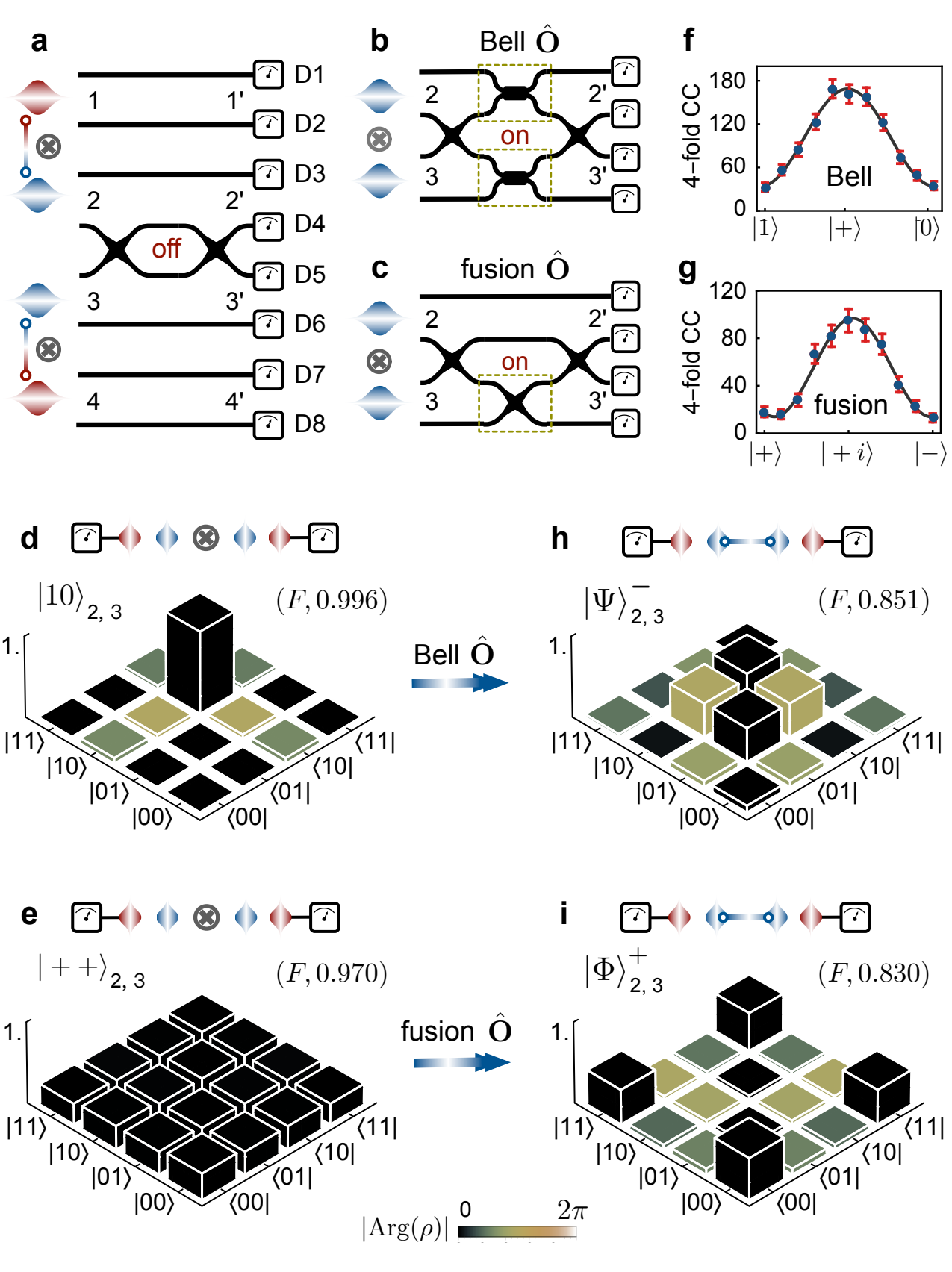
a
D1
D2
D3
D4
D5
D6
D7
D8
1
1'
2
2'
off
3
3'
4
4'
b
Bell $\hat{O}$
2
2'
on
3
3'
c
fusion $\hat{O}$
2
2'
on
3
3'
f
4–fold CC
180
120
60
0
Bell
$|1\rangle$
$|+\rangle$
$|0\rangle$
g
4–fold CC
120
80
40
0
fusion
$|+\rangle$
$|+i\rangle$
$|-\rangle$
d
$|10\rangle_{2,3}$
$(F, 0.996)$
1.
|11⟩
|10⟩
|01⟩
|00⟩
⟨11|
⟨10|
⟨01|
⟨00|
Bell $\hat{O}$
h
$|\Psi\rangle^{-}_{2,3}$
$(F, 0.851)$
1.
|11⟩
|10⟩
|01⟩
|00⟩
⟨11|
⟨10|
⟨01|
⟨00|
e
$|++\rangle_{2,3}$
$(F, 0.970)$
1.
|11⟩
|10⟩
|01⟩
|00⟩
⟨11|
⟨10|
⟨01|
⟨00|
fusion $\hat{O}$
i
$|\Phi\rangle^{+}_{2,3}$
$(F, 0.830)$
1.
|11⟩
|10⟩
|01⟩
|00⟩
⟨11|
⟨10|
⟨01|
⟨00|
$|\mathrm{Arg}(\rho)|$
0
2π

a

i)

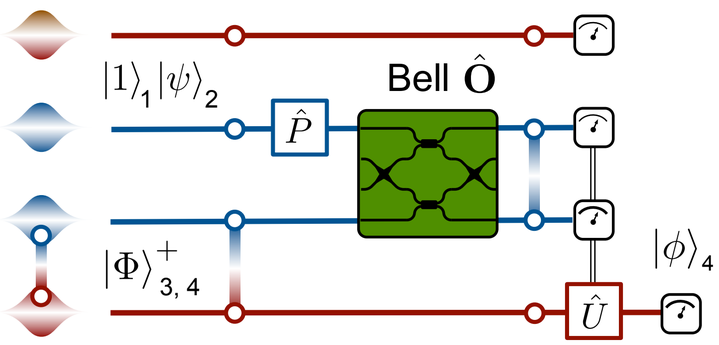

ii)

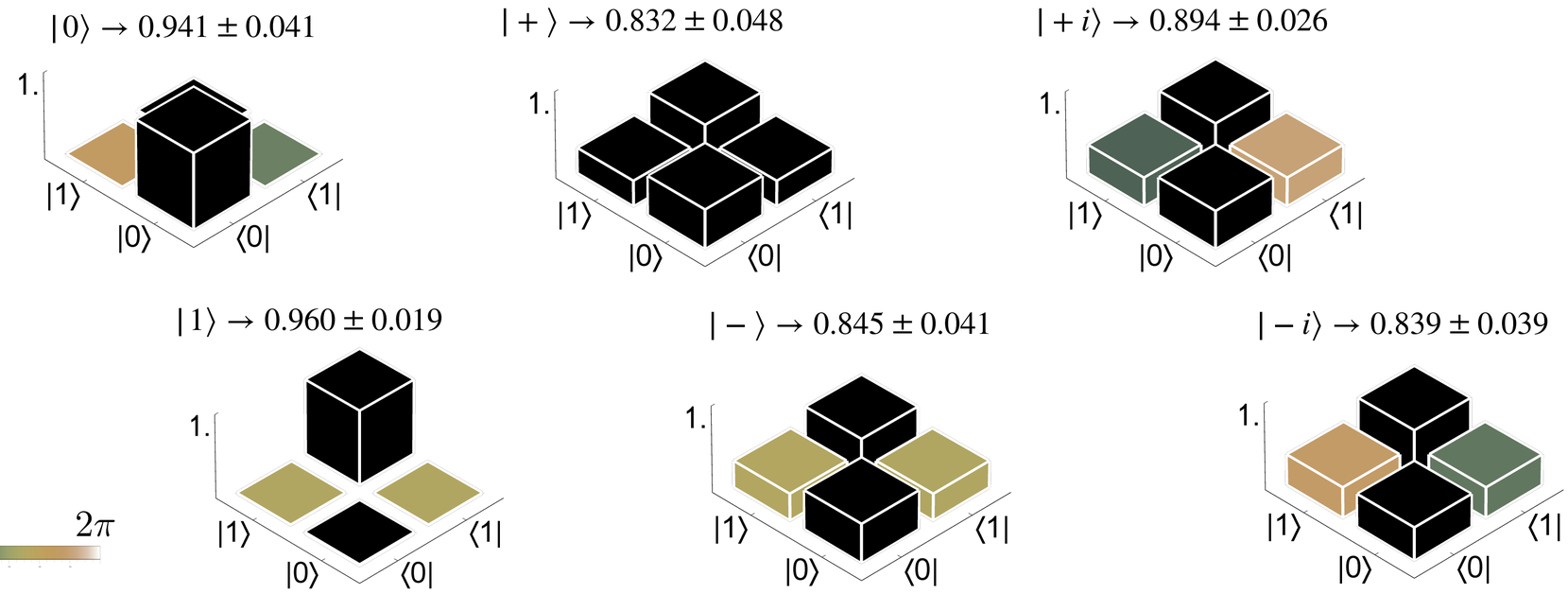

b

i)

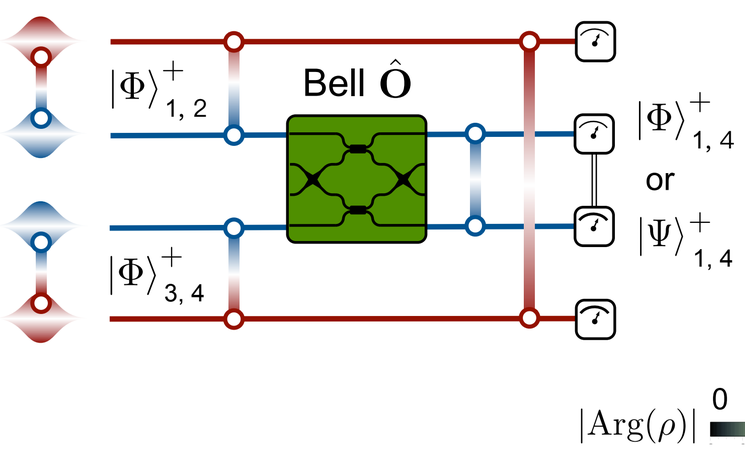

ii)

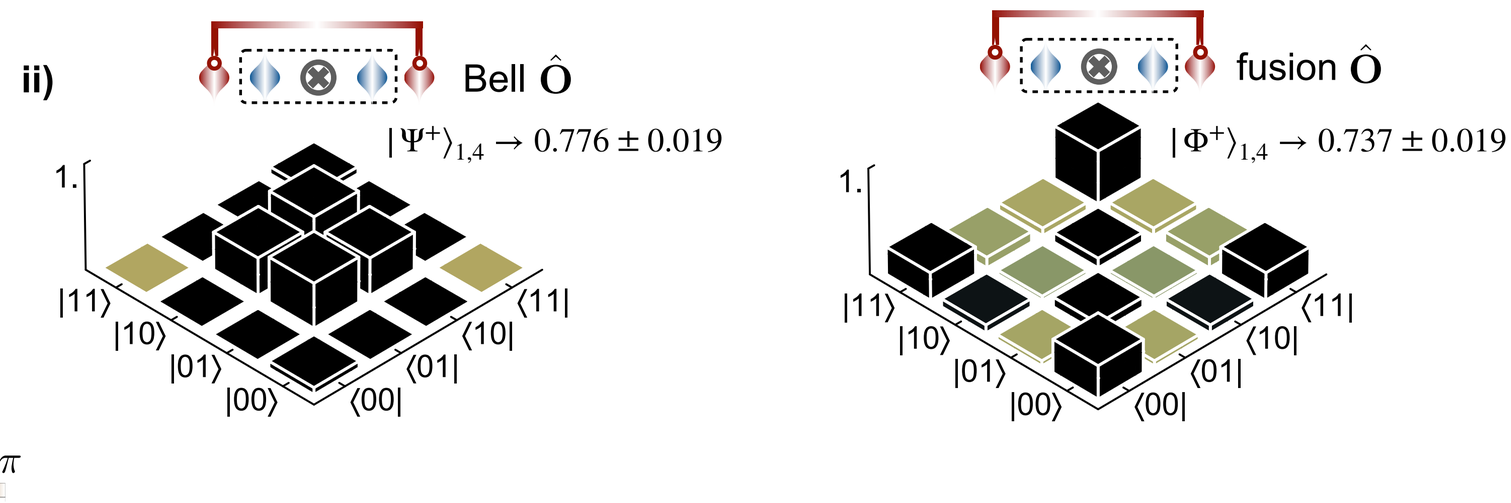

c

i)

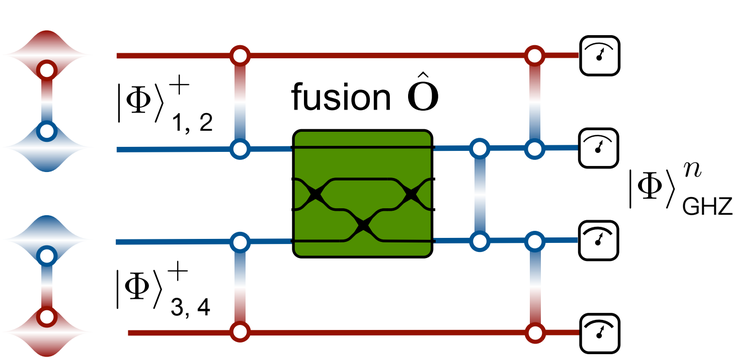

ii)

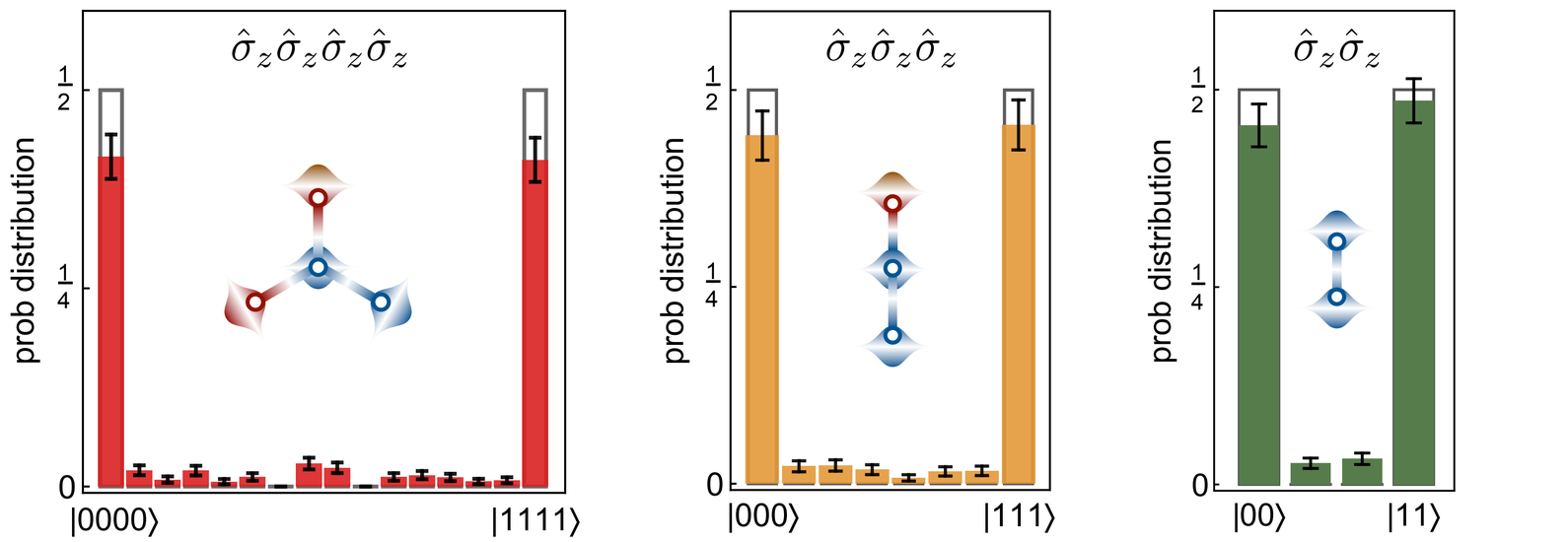

iii)